Promotional removal of HCHO from simulated flue gas over Mn-Fe oxides modified activated coke

Xueyu Du[a,b], Caiting Li[a,b,*], Lingkui Zhao[a,b,c], Jie Zhang[a,b], Lei Gao[a,b], Jingjing Sheng[a,b], Yaoyao Yi[a,b], Jiaqiang Chen[a,b], Guangming Zeng[a,b]

[a] College of Environmental Science and Engineering, Hunan University, Changsha 410082, PR China
[b] Key Laboratory of Environmental Biology and Pollution Control (Hunan University), Ministry of Education, Changsha 410082, PR China
[c] College of Environmental Science and Resources, Xiangtan University, Xiangtan 411105, PR China

ABSTRACT

A series of Mn_xFe_y/AC catalysts synthesized by impregnation method were investigated on the efficient and stable removal of HCHO in the fix-bed reactor. Extensive characterizations, BET, SEM, XRD, H_2-TPR, XPS and FT-IR, were conducted to study the physicochemical properties, HCHO oxidation and surface reaction of catalysts. The optimal $Mn_{0.75}Fe_{6.02}/AC$ showed enhanced HCHO removal efficiency of 98.30%, as well as excellent performance for simultaneous removal of HCHO (89.96%) and Hg^0 (77.51%). NO and SO_2 balanced in N_2 would inhibit the removal of HCHO, while the addition of 6% O_2 weakened the negative effect of SO_2 and NO + 6% O_2 facilitated the removal of HCHO. Besides, the slight promotion effect of water vapor was contributed to the regeneration of consumed $-OH$ via the activation of surface oxygen by adsorbed H_2O. Characterization results indicated that $Mn_{0.75}Fe_{6.02}/AC$ possessed larger BET surface area, well-developed porosity and better dispersion of active components. $Mn_{0.75}Fe_{6.02}/AC$ exhibited higher reducibility due to the synergistic effect between MnO_x and FeO_x, and the interaction between Mn-Fe oxides and AC support. At the same time, the oxygen-containing functional groups (C-O-, COO), abundant active surface oxygen and –OH facilitated both adsorption and oxidation of HCHO. Besides, the formate and carbonate intermediates formed on the surface of $Mn_{0.75}Fe_{6.02}/AC$ in HCHO removal process, which could be further oxidized into CO_2 and H_2O. On the basis of above investigations, the mechanism of enhanced HCHO catalytic removal over Mn_xFe_y/AC was proposed.

1. Introduction

Volatile organic compounds (VOCs) released from anthropogenic sources are an important contributor of atmospheric pollution. Coal combustion has been considered as a major source of anthropogenic VOCs emissions due to the enormous demand of coal in industrial manufacturing. As one of the hazardous VOCs, formaldehyde (HCHO) has been widely considered as a great threat to the human health [1,2]. Besides, HCHO can also react with NO_x and make contribution to photochemical smog due to its strong photochemical activity [3,4]. Therefore, it is urgent to develop efficient technologies for HCHO removal.

To meet the stringent environmental regulations, various technologies, such as adsorption [5], condensation [6], photo-catalysis [7], catalytic oxidation [8], plasma technology [9], and biological filtration [10], have been developed to eliminate the emission of HCHO. Among them, catalytic oxidation is considered as a promising technology due

to its saving of energy and the minimization of the generation of toxic by-products [11].

In recent decades, the main catalysts for adsorption and catalytic oxidation of HCHO are supported noble metals or transition metal oxides. These catalysts are highlighted to be an effective and promising technology with high efficiency and low energy consumption. In particular, various metal oxides supports, including TiO_2 [12], MnO_x [13], CeO_2 [14], FeO_x [3,15], ZrO_2 [16], Al_2O_3 [17] and the metal composites like CeO_2-Co_3O_4 [18], MnO_x-CeO_2 [19] and In_2O_3-SnO_2 [20] are usually used for HCHO oxidation, and could facilitate the activity of deposited active components due to their high dispersion, strong redox properties of the support and the synergy effect with supported metal oxides. However, several shortcomings of current employed metal oxides supports, such as non-uniform structure, uncontrollable size and shape, as well as high cost, have prevented their application. Therefore, porous supports with regular structure have attracted much attention [21–26]. As a kind of carbon based material with porous structure,

activated coke (AC) possesses considerable environmental and economic benefits on account of its rich source, high mechanical strength, lower cost and better regeneration performance [27,28]. Compared with activated carbon, AC is comprised mainly of macropore and mesopore instead of micropore, which reduces significantly the impact of internal diffusion on the general rate of adsorption and catalytic processes. Hence, AC is usually considered as a suitable support used for the decomposition of VOCs into H_2O due to its hydrophilic character. Additionally, AC could be used for the removal of numerous pollutants such as SO_2 [29], H_2S [30], NO_x [31] and Hg^0 [32–34]. The literatures [35,36] reported that AC has been also exploited in treating organic pollutants in wastewater from industrial process.

Nevertheless, the removal capacity of virgin AC towards HCHO is restricted by its limited physicochemical property such as activated site and surface area. It has been reported that the carbon-based material loaded with metal oxides possessed both high adsorption and catalytic ability [37]. Therefore, the modification of AC by metal oxides seems to be a potential approach to improve the activity of AC to a great extent [32,38,39].

As previously reported [8,40,41], some non-noble metal oxides with fast electron transference and variable valences, such as manganese oxides and iron oxides, have been used as active phase owe to their low cost, wide availability and high resistance to sulfur and chlorine. Significantly, manganese-based catalysts have been focused as promising, inexpensive, environmental friendly and effective catalysts for HCHO removal. For example, large oxygen storage capacity of manganese oxides caused by the ability to switch oxidation states ensures higher activity for VOCs removal [42]. As is reported, manganese oxides have been proved to be more effective than some transition metal oxides, such as TiO_2, CeO_2, or even some binary oxides for HCHO removal [43]. It is well known that Mn has variable valence states from -3 to $+7$ due to its electronic structure $3d^5 4s^2$ [8]. On one hand, the manganese oxides are able to mobilize electrons, thus generating the mobile-electron environment required by redox reaction. On the other hand, their redox properties are greatly enhanced with incorporation of other elements [44]. Currently, Fe was widely applied and exhibited good performance for VOCs oxidation. It was demonstrated that Fe^{3+} sites could facilitate the formation of O_2^{2-} species that are vital for the activation and oxidation of VOCs [45]. The capability of Fe containing oxide to generating active oxygen species has also been highlighted [46]. Therefore, ideas for the co-modification of MnO_x and FeO_x over AC (Mn_xFe_y/AC) to improve the activity are encouraged. Unfortunately, there were still few reports about using Mn_xFe_y/AC for the removal of HCHO from simulated flue gas. In addition, the mechanism of enhanced HCHO removal over the catalyst was still not very clear.

Therefore, in this paper, a series of Mn_xFe_y/AC samples were investigated for HCHO removal, with emphasis on four aspects: (i) removal performance of HCHO over Mn_xFe_y/AC and their potential in practice application; (ii) the simultaneous removal of Hg^0 and HCHO; (iii) the physicochemical and structural properties; (iv) the mechanism of HCHO removal. The objective of the work is to give an in-depth exploration in the relationship between the physicochemical properties and catalytic activity of Mn_xFe_y/AC, and develop an eco-friendly and effective catalyst for HCHO removal.

2. Experimental section

2.1. Samples preparation

A series of Mn_xFe_y/AC (where x denotes the $Mn/(Mn + Fe)$ molar ratio in Mn-Fe oxides, while y denotes the total mass percent of metal Mn-Fe on Mn_xFe_y/AC) samples have been prepared by equivalent volume impregnation. Initially, the virgin AC (D = 3 mm and L = 4–6 mm, Alxa League Ke'xing Carbon industry) was washed with deionized water repeatedly and then dried at 105 °C for 12 h. Secondly, appropriate amounts of 50 wt.% $Mn(NO_3)_2$ solution and $Fe(NO_3)_3 \cdot 9H_2O$

were dissolved in deionized water and the AC was impregnated in the solution at room temperature for 24 h. For example, as for $Mn_{0.75}Fe_{3.30}/AC$, 2.156 mL 50 wt.% $Mn(NO_3)_2$ solution and 1.2471 g $Fe(NO_3)_3 \cdot 9H_2O$ were dissolved into deionized water as impregnation solution. The obtained precursor was then dried at 105 °C for 12 h and finally calcined at 500 °C for 4 h under N_2 atmosphere. The metal loading value, described as y, was equal to 0.65%, 1.97%, 3.30%, 4.65%, 6.02% and 7.42%. Besides, to identify the effect of the molar ratio of $Mn/(Mn + Fe)$ on physicochemical properties of samples, the value of x was set as 0, 0.15, 0.3, 0.5, 0.75, 0.9, 1.

2.2. Samples characterization

To study the basic characters of virgin AC, the proximate analysis of virgin AC were measured by Chinese National standards (GB/T 212-2008). And the ultimate analysis of virgin AC was conducted using the Elementar Analysensystem GmbH vario (Elementar Ltd Corp, Germany).

The actual content of metal doping over AC was measured by Inductively Coupled Plasma-Atomic Emission Spectrometry (ICP-AES, SPECTRO BLUE SOP, Germany).

The pore structure including the Brunauer-Emmett-Teller specific surface area (S_{BET}), pore volume and average pore size was determined by standard nitrogen adsorption on a Micromeritics Tri-star 3020 analyzer (Micromeritics Instrument Crop, USA). And samples were previously degassed at 120 °C before BET measurement.

The scanning electron microscopy (SEM) micrographs ($\times 10,000$) of all samples were collected on a JSM-6700F (Japan) instrument.

The X-ray diffraction (XRD) patterns were obtained on a Rigaku rotaflex D/Max2500 powder diffractometer (Rigaku, Japan) at room temperature with Cu-Kα radiation at 40 KV and 250 mA. The diffraction line positions were determined with a step of 0.02° in a scanning range of 10–80° (2θ).

To identify the redox properties of samples, the temperature-programmed reduction of hydrogen (H_2-TPR) was performed on an AutoChem 2090 automated chemisorption analyzer (Micromeritics Instrument Crop, USA). For the analysis, about 100 mg of samples were pretreated under N_2 flow at 300 °C for 30 min and then cooled down to the room temperature. The reduction measurement was carried out from the room temperature to 900 °C with a heating rate of 10 °C/min under 5% H_2-Ar (40 mL/min) atmosphere.

The X-ray photoelectron spectroscopy (XPS) analyses were conducted on a K-Alpha 1063 spectrometer (Thermo Fisher Scientific, UK) to study the chemical states of the constituent elements. All spectra were recorded using an Al Kα X-ray radiation source. The charge-shifted spectra were referenced to C 1s line position at 284.6 eV.

The Fourier Transform Infrared Spectroscopy (FT-IR) was collected in range of 500–4000 cm^{-1} on a FTIR-8400 S IRprestige-21 (SHIMADZU, Japan) apparatus at a spectral resolution of 2 cm^{-1} to characterize the intermediates and products during HCHO removal on sample surface. Prior to each measurement, the sample was pretreated at 250 °C in a pure N_2 gas flow of 500 mL/min for 1 h for the removal of impurity and moisture adsorbed on sample and subsequently cooled down to room temperature. Then the pretreated sample was exposed to the corresponding gas atmosphere of HCHO (120 ppm HCHO balanced in N_2) at room temperature and HCHO + O_2 (120 ppm HCHO, 6% O_2 and balanced N_2) at room temperature and at optimal reaction temperature, for 2 h to be saturated, respectively.

2.3. Experimental setup and procedure

The experiments of the removal of HCHO on Mn_xFe_y/AC were carried out in a continuous flow-type apparatus, consisting of a continuous simulated flue gas supplying system, a fixed-bed quartz reactor (52 mm inner diameter × 870 mm length) and a gas analyzer system, as shown in Fig. 1. The feed of gas-phase HCHO to the reactor was
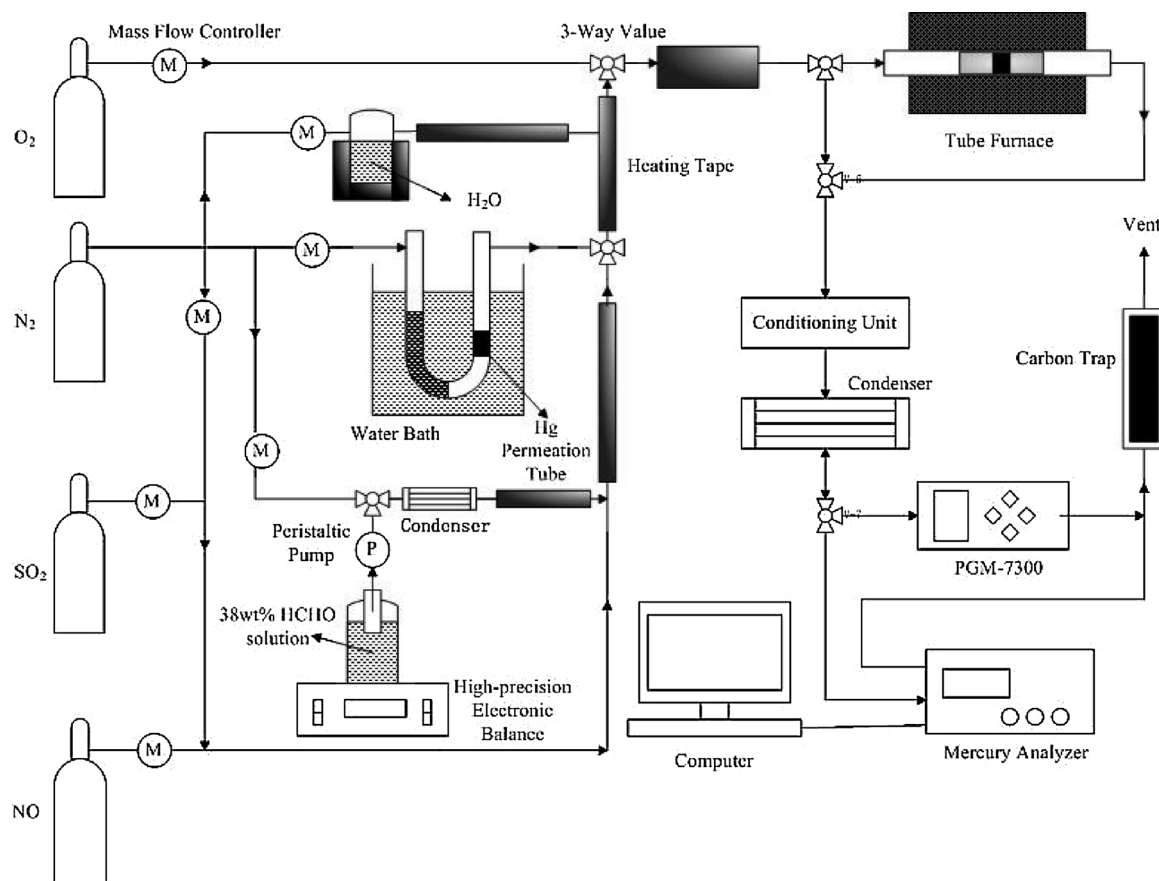
Fig. 1. Schematic diagram of the experimental setup.

performed by controlling a peristaltic pump to inject 38 wt.% formaldehyde solution into Teflon tube wrapped with temperature-controlled heating tape. Then 100 mL/min N_2 took generated gas-phase HCHO alone through the condensing apparatus to remove the water vapor, and then mixed with the simulated flue gas. The Hg^0 vapor-generating device was made up of an elemental mercury permeation tube (VICI Metronics, USA) and a water bath with a tunable temperature. A feed of 120 ppm HCHO, 6 vol.% O_2, 90 μg/m^3 Hg^0 (when used) and the balance of N_2 were controlled by mass flow controllers respectively and the total flow rate of the flue gas was maintained at 500 mL/min, corresponding to a gas hourly space velocity (GHSV) of 2500 h^{-1}. For each test, 20 g sample was placed in the middle of the quartz tube horizontally. The concentration of inlet (HCHO$_{in}$) and outlet (HCHO$_{out}$) HCHO were measured by PGM7300 analyzer (RAE, USA), and the selectivity of HCHO over Mn_xFe_y/AC was calculated combining with the concentration of outlet CO_2 which was monitored by PGA-650 (Phymetrix, USA). The inlet ($[Hg^0]_{in}$) and outlet Hg^0 ($[Hg^0]_{out}$) concentration were measured using an online RA-915M mercury analyzer (LUMEX Ltd, Russia). The oxidation of mercury was measured by the difference of Hg^0 concentration through the mercury transformation system and $[Hg^0]_{out}$, as depicted in Tao et. al [32]. After the desired inlet concentration has been established for 30 min, the experimental gas stream was introduced to pass through each sample until the HCHO$_{out}$ reached stable in pre-experiment. Prior to testing the HCHO and Hg^0 removal efficiency, blank test was conducted to avoid any influence of the reactor. And the reaction time for each test was 6 h.

The removal efficiency of HCHO (E_{HCHO}) and conversion to CO_2 (S_C) was calculated from the equation below:

$$E_{HCHO}(\%) = \frac{\Delta HCHO}{HCHO_{in}} = \frac{HCHO_{in} - HCHO_{out}}{HCHO_{in}} \times 100\% \qquad (1)$$

$$S_C(\%) = \frac{CO_2}{HCHO_{in} \times E_{HCHO}} \times 100\% \qquad (2)$$

where HCHO$_{in}$ and HCHO$_{out}$ represent HCHO concentration (ppm) at the inlet and outlet of the fixed-bed reactor, respectively.

The mercury removal efficiency (E_{Hg}) was defined as:

$$E_{Hg}(\%) = \frac{\Delta Hg^0}{[Hg^0]_{in}} = \frac{[Hg^0]_{in} - [Hg^0]_{out}}{[Hg^0]_{in}} \times 100\% \qquad (3)$$

$$E_{oxi}(\%) = \frac{[Hg^0]_{oxi}}{[Hg^0]_{in}} \times 100\% \qquad (4)$$

where $[Hg^0]_{in}$ is the inlet Hg^0 concentration and $[Hg^0]_{out}$ is the outlet Hg^0 concentration (μg/m^3), and $[Hg^0]_{oxi}$ is the outlet Hg^{2+} concentration (μg/m^3).

3. Results and discussion

3.1. Textural, structural and morphologic characterizations

3.1.1. Proximate, ultimate analysis and ICP-AES

As shown in Table 1, the basis characters of virgin AC were investigated by proximate and ultimate analysis. The ultimate composition of virgin AC is 86.88% C + 0.70% H + 11.11% O + 0.68% N + 0.63% S, and the proximate analysis indicated that the virgin AC was comprised of 2.57% moisture, 12.67% ash, 22.74% volatile and 62.02% fixed carbon.

The actual content of metal in different samples was measured using ICP-AES. As summarized in Table 2, the actual content of metal was slightly lower than the theoretical value for all samples. The slight difference might be attributed to the inevitable loss of metal nitrate precursor during the impregnation process.

Table 1
Proximate and ultimate analysis of virgin AC (air-dry basis).

Samples	Proximate analysis (wt.% ad)				Ultimate analysis (wt.% ad)				
	M	A	V	FC[a]	C	H	O[a]	N	S
Virgin AC	2.57	12.67	22.74	62.02	86.88	0.70	11.11	0.68	0.63

[a] by difference M % + A % + V % + FC[a] % = 100%; C % + H % + O[a] % + N% + S % = 100%.

Table 2
The content (wt.%) of metal in samples obtained by ICP-AES.

Sample	Mn content (wt.%)		Fe content (wt.%)	
	nominal content	actual content	nominal content	actual content
$Fe_{3.30}$/AC	–	–	3.30	3.18
$Mn_{0.30}Fe_{3.30}$/AC	0.98	0.87	2.32	2.21
$Mn_{0.50}Fe_{3.30}$/AC	1.64	1.51	1.66	1.58
$Mn_{0.75}Fe_{3.30}$/AC	2.46	2.32	0.84	0.79
$Mn_{3.30}$/AC	3.30	3.21	–	–
$Mn_{0.75}Fe_{0.65}$/AC	0.49	0.41	0.17	0.10
$Mn_{0.75}Fe_{6.02}$/AC	4.49	4.34	1.53	1.41

3.1.2. BET

Textural properties of virgin AC and $Mn_{0.75}Fe_y$/AC, including BET specific surface area, pore volume and pore size, were investigated by N_2 adsorption-desorption measurement. As shown in Table 3, the co-modification of MnO_x and FeO_x could increase the surface area and pore volume of AC to a certain extent. It could be found that the Mn-Fe modified AC except $Mn_{0.75}Fe_{7.42}$/AC, possessed higher BET surface area and pore volume than virgin AC. At the same time, BET surface area and pore volume increased as the loading of metal Mn-Fe increased from 0.65% to 6.02%, which increased from 237.62 m^2/g and 0.121 cm^3/g to 272.21 m^2/g and 0.145 cm^3/g, respectively. It might be attributed to a number of new pores formed during impregnation and calcination [34]. Nevertheless, with further increasing the active components loadings, a marked reduction in the BET surface area and pore volume was observed. According to Tao et al. [32], the decrease might be ascribed to that an excess of metal oxides loaded on AC formed the agglomeration to cover the external surface of AC, thus blocking a number of pores. In particular, $Mn_{0.75}Fe_{6.02}$/AC possessed the highest specific surface area and pore volume. In general, larger BET surface area the material possessed, there were more active sites and larger interface for the adsorption and the following oxidation HCHO on Mn_xFe_y/AC catalysts, which gave rise to a high catalytic activity [47].

3.1.3. SEM

The external morphology and microstructure of selected samples were characterized by SEM, as depicted in Fig. 2. Compared with virgin AC, the morphological characteristics of AC have been changed after loading with Mn-Fe oxides, which were homogeneously dispersed on the surface of AC at micrometric scale. In addition, more and more particles were observed over surface of samples with the increase of Mn-Fe loading below 3.30%. It is noted that rough surface of

Table 3
BET surface and pore parameters of the different samples.

Samples	BET surface area (m^2/g)	Pore volume (cm^3/g)	Average pore diameter (nm)
AC	237.62	0.121	2.038
$Mn_{0.75}Fe_{0.65}$/AC	248.14	0.125	2.017
$Mn_{0.75}Fe_{3.30}$/AC	265.83	0.130	1.948
$Mn_{0.75}Fe_{6.02}$/AC	272.21	0.145	2.127
$Mn_{0.75}Fe_{7.42}$/AC	218.29	0.117	2.155

$Mn_{0.75}Fe_{4.65}$/AC and $Mn_{0.75}Fe_{6.02}$/AC exhibited some interlamellar structure (Fig. 2(e)–(f)), especially for $Mn_{0.75}Fe_{6.02}$/AC, thus increasing its BET surface area, which endowed the samples more efficient in adsorbing HCHO and other gaseous components [48]. However, compared with $Mn_{0.75}Fe_{6.02}$/AC, there were more agglomerates rather than distinct interlamellar structure observed over $Mn_{0.75}Fe_{7.42}$/AC, which might be the result of excess active components deposition. The appearance of agglomerates led to the blockage of pores and a lower specific surface area, which was in accordance with BET results (Table 3).

3.1.4. XRD

As shown in Fig. 3A, the XRD measurement was performed to identify the crystal structures of the $Mn_{0.75}Fe_y$/AC samples with different metal loadings, together with virgin AC. It could be seen that the diffraction lines for SiO_2 ($2\theta = 28.899°$, $32.220°$ and $36.040°$, PDF-ICDD 18-1170) were detected over virgin AC. On one hand, the primary peaks at $2\theta = 26.603°$, $44.464°$ (PDF-ICDD 25-0248) corresponding to carbon were observed over all samples, revealing that the microstructure of AC was remained to a certain extent after impregnation. On the other hand, with the doping of Mn-Fe oxides over AC, the intensity of the characteristic peaks of carbon decreased with increasing metal oxides content, suggesting that the loading of metal oxides over AC changed the natural structure of AC. The results above also could be inferred that the interaction may exist between Mn-Fe oxides and AC, as demonstrated in BET, SEM and XPS. Interestingly, the diffraction peaks at $2\theta = 32.315°$, $36.085°$, $44.440°$ and $59.840°$ were ascribed to Mn_3O_4 (PDF-ICDD 24-0734), and the diffraction peak at $2\theta = 40.547°$ was attributed to MnO (PDF-ICDD 07-0230), while no related peaks of Fe_2O_3 or FeO were observed on the surface of $Mn_{0.75}Fe_y$/AC, suggesting that the content of iron oxides was too low to form crystalline phase according to monolayer dispersion theory [49]. Besides, the particle size of metal oxides increased with the increasing loading value. The particle size of Mn_3O_4 estimated by the Scherrer equation and MDI Jade was 12.32nm and 12.09nm for $Mn_{0.75}Fe_{6.02}$/AC and $Mn_{0.75}Fe_{4.65}$/AC, respectively. Compared with $Mn_{7.42}$/AC, after the doping of FeO_x, the intensity of peaks assigned to Mn_3O_4 weakened distinctly (Fig. 3B), demonstrating the existence of FeO_x led to the lower crystallinity or smaller crystallite size of MnO_x, and presumably the subsequent high catalytic activity.

3.2. Redox properties

3.2.1. H_2-TPR

As is recognized, the catalytic oxidation of VOCs on catalysts where metal oxides act as the active components occurred through the oxidation of organic molecule by the lattice oxygen originating from metal oxides and subsequently the reoxidation of the catalyst by gas-phase oxygen [50]. To keep the mechanism proceeding, the redox pairs of supported metal oxides in different oxidation states are essential during the elimination of VOCs. As illustrated in Fig. 4, for virgin AC, the H_2-TPR profile revealed two overlapping peaks characterized by apparent maxima at 485 and 658 °C approximatively. The first peak at about 485 °C might be assigned to the reduction of surface oxygen species, and the higher peak corresponds to the gasification of the carbon support [51,52]. However, after the loading of MnO_x, $Mn_{6.02}$/AC
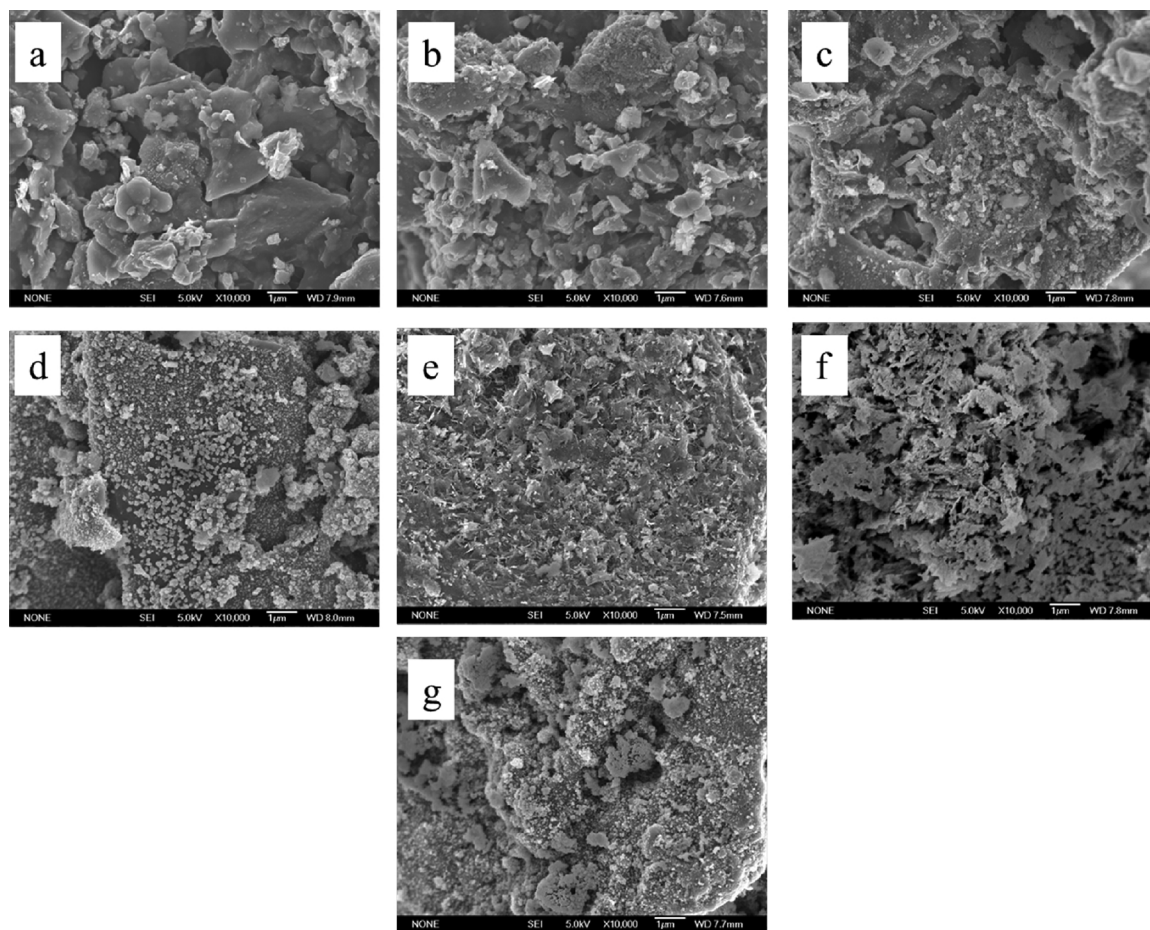
Fig. 2. SEM images ($\times$10,000) of (a) virgin AC, (b) $Mn_{0.75}Fe_{0.65}/AC$, (c) $Mn_{0.75}Fe_{1.97}/AC$, (d) $Mn_{0.75}Fe_{3.30}/AC$, (e) $Mn_{0.75}Fe_{4.65}/AC$, (f) $Mn_{0.75}Fe_{6.02}/AC$, (g) $Mn_{0.75}Fe_{7.42}/AC$.

exhibited another two peaks centered at 275 and 500 °C, representing the initial reduction of amorphous MnO_2 to Mn_3O_4 and the further reduction of Mn_3O_4 to MnO, as well as the reduction of surface oxygen, while the broad higher peak at 675 °C might be partly contributed to the reduction of lattice oxygen [47]. For $Fe_{6.02}/AC$ sample, the peak at 380 °C can be attributed to the reduction of Fe_2O_3 to Fe_3O_4, whereas the higher temperature reduction peak at 550 °C owed to the transition of Fe_3O_4 to FeO and the reduction of surface oxygen [3]. Compared with $Mn_{6.02}/AC$ and $Fe_{6.02}/AC$, four peaks of $Mn_{0.75}Fe_{6.02}/AC$ appeared at approximately 265, 470, 560 and 675 °C, corresponding to a superposition of the individual peaks of them. The peaks ascribed to the reduction of $MnO_2 \rightarrow Mn_2O_3 \rightarrow MnO$ shifted to lower temperature at 265 and 470 °C, respectively. And the peak at 560 °C might be the result of the reduction of Fe^{3+} and the surface oxygen. It could be seen that the reduction peaks shifted towards lower temperature, manifesting the strong interaction of MnO_x-FeO_x, as well as the interaction between active components and support. In addition, the strong interaction between MnO_x and FeO_x can improve the mobility of active oxygen species over the surface of catalysts, which is conducive for the destruction of VOCs and the further oxidation of byproducts. The lower reduction temperature of sample is, the higher reducibility the sample owns, causing the formation of more oxygen vacancies [53]. Therefore, $Mn_{0.75}Fe_{6.02}/AC$ was endowed with the capacity of producing more oxygen vacancies with the aid of FeO_x than $Mn_{6.02}/AC$. And then gas-phase O_2 was easier to fill the oxygen vacancies, thus generating more active surface species [54].

3.2.2. XPS

The chemical states of the surface elements (C, O, Mn, Fe) over samples were elucidated by XPS measurement. Fig. 5A illustrates the

C1s XPS spectra. The characteristic peaks occurring in graphitic carbon (284.6–285.1 eV), carbon presenting in alcohol or ether groups (286.3–287.0 eV), carbonyl groups (287.5–288.1 eV), carboxyl or ester groups (289.3–290.0 eV) and shake-up satellite peaks due to π-π^* transitions in aromatic rings (291.2–292.1 eV) could be found [55]. With metal oxides doping, all peaks shifted to higher binding energy, and the ratio of C–C and O–C=O increased from 57.19% and 1.81% for virgin AC to 74.55% and 3.97%, respectively, while C–O– and C=O showed a decrease of 18.72% and 2.34% (Table 4). The acidity of Mn $(NO_3)_2$ and $Fe(NO_3)_3$ solution during the impregnation may give rise to the generation of acidic O–C=O groups, as reported in the literature [56]. Besides, the heating of AC under N_2 atmosphere during calcination led to a drop in the concentration of surface oxygen functional groups caused by desorption of surface chemisorbed oxygen, thus an increase of C–C.

Additionally, the XPS spectra for O1s of samples could be fitted in three peaks at 529.2–530.2 eV, 531.3–532.3 eV and 532.7–533.5 eV, corresponding to lattice oxygen (O_L), surface adsorbed oxygen, hydroxyl group and oxygen vacancies (O_{OH}), and surface oxygen in adsorbed water species (O_W) [57,58], respectively. Compared with virgin AC, the peaks of O_L and O_{OH} of modified AC shifted to higher binding energy, which might be contributed to the changes in the chemical environment of oxygen atoms after the loading of metal oxides [59]. In other words, a part of C atoms bonding with O were replaced by Mn and/or Fe atoms. Nevertheless, the co-modified AC owned lower binding energy of O_L than $Mn_{6.02}/AC$ and $Fe_{6.02}/AC$, which acted as an oxygen storage role in metal oxide system [59]. Besides, the ratio of O_{OH}/O_T ($O_T = O_L + O_{OH} + O_W$) over $Mn_{0.75}Fe_{.02}/AC$ (57.51%) was higher than that of $Mn_{6.02}/AC$ (37.13%) and $Fe_{6.02}/AC$ (43.08%) (Table 4), indicating the interaction between MnO_x and FeO_x was in

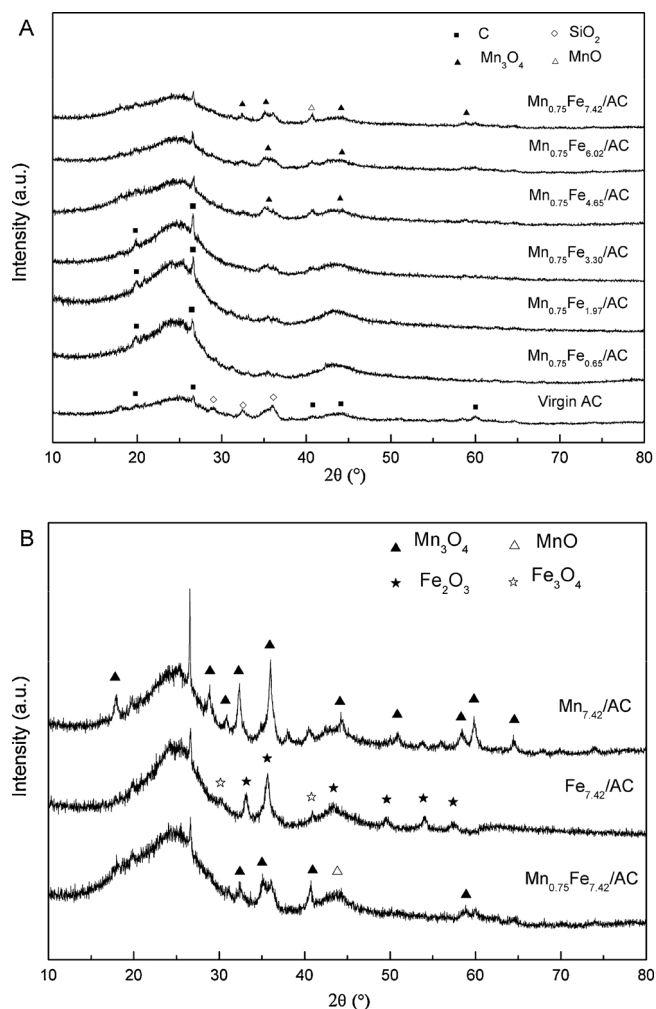**Fig. 3.** XRD patterns of (A) $Mn_{0.75}Fe_y/AC$, (B) $Mn_{7.42}/AC$, $Fe_{7.42}/AC$ and $Mn_{0.75}Fe_{7.42}/$AC.

H and surface adsorbed oxygen, was beneficial for the adsorption and oxidation of HCHO [53].

As seen from the Mn2p core spectra in Fig. 5C, for $Mn_{6.02}/AC$, the peaks at 641.36 eV, 642.92eV, 645.88 eV are ascribe to Mn^{2+}, Mn^{3+} and Mn^{4+}, respectively [8]. After the doping of FeO_x, all peaks shifted to lower binding energy, and the ratios of Mn^{4+}/Mn^{3+} and $(Mn^{4+} + Mn^{3+})/Mn^{2+}$ increased (Table 4), suggesting that the incorporation of FeO_x could facilitate the generation of Mn atoms with high valance on sample surface. As reported [61], Mn^{4+} can directly oxidize the adsorbed reactant, and the Mn^{3+} also plays an important role in oxidation with the presence of O_2. Therefore, the higher values of $(Mn^{4+} + Mn^{3+})/Mn^{2+}$ and Mn^{4+}/Mn^{3+} are favorable for HCHO oxidation.

As shown in Fig. 5D, two main asymmetric peaks located at 711.0 and 725.0 eV correspond to $Fe2p_{3/2}$ and $Fe2p_{1/2}$, respectively. For $Fe2p_{3/2}$, the binding energies at 710.2–710.4 eV and 711.3–712.1 eV are ascribed to the Fe^{3+} cations in different forms, and another peak at 712.3–713.3 eV is attributed to Fe^{III}-OH. Besides, the shake-up satellite peak at about 719.0 eV is the fingerprint of Fe^{3+}. The results revealed that Fe^{3+} was the only oxidation state existing on sample surface, while Fe^{2+} existed inside the catalysts could not be detected by XPS characterization [8]. After the doping of MnO_x, the ratio of Fe^{3+}/Fe^{III}-OH decreased from 1.53 to 1.17 (Table 4), suggesting the addition of MnO_x over $Mn_{0.75}Fe_{6.02}/AC$ induced the formation of Fe^{3+} bonded with hydroxyl groups, which was in well agreement with the increase of O_{OH}.

3.3. Catalytic performance

The removal performances of HCHO over $Mn_xFe_{3.30}/AC$ in simulated flue gas were investigated at the temperature of 150–330 °C. As shown in Fig. 6, virgin AC showed the lowest HCHO removal efficiency (E_{HCHO}) of 60–70%. Obviously, the addition of MnO_x or/and FeO_x over AC significantly enhanced the HCHO removal activity of catalysts, and a promotional impact was obtained over $Mn_xFe_{3.30}/AC$. E_{HCHO} initially increased with the increasing temperature from 150 °C to 300 °C, especially a marked increase during 210–270 °C, and then leveled off finally. A higher temperature endowed the reactants with more kinetic energy, thus promoted the oxidation of HCHO. Among the catalysts, $Mn_{0.75}Fe_{3.30}/AC$ exhibited the best performance in HCHO removal, reaching excellent removal efficiency above 85% with a broad reaction temperature window of 210–330 °C and the maximum of 96.75% at 300 °C. Furthermore, compared with single metal oxides doping, $Mn_xFe_{3.30}/AC$ was more effective for the removal of HCHO.

As a crucial factor, the content of metal oxides affects not only dispersion and aggregation of Mn_xFe_y/AC, but also its crystallinity and
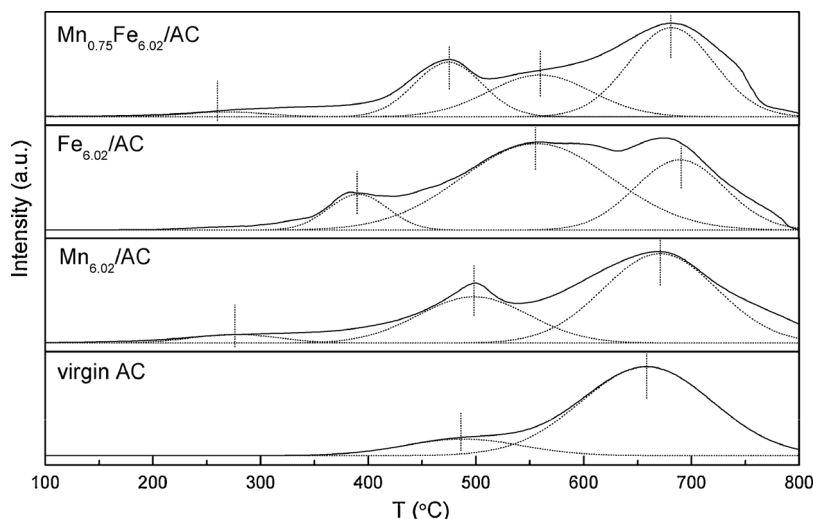
favor of the generation of O_{OH} on the surface of samples, which was consistent with H_2-TPR (Fig. 4). On one hand, the surface adsorbed oxygen could facilitate the adsorption of gas-phase oxygen from simulated flue gas on the surface with high activity and mobility [60]. On the other hand, the generation of −OH, via the covalence bond between

Fig. 4. H_2-TPR profiles of virgin AC, $Mn_{6.02}/AC$, $Fe_{6.02}/AC$ and $Mn_{0.75}Fe_{6.02}/AC$.
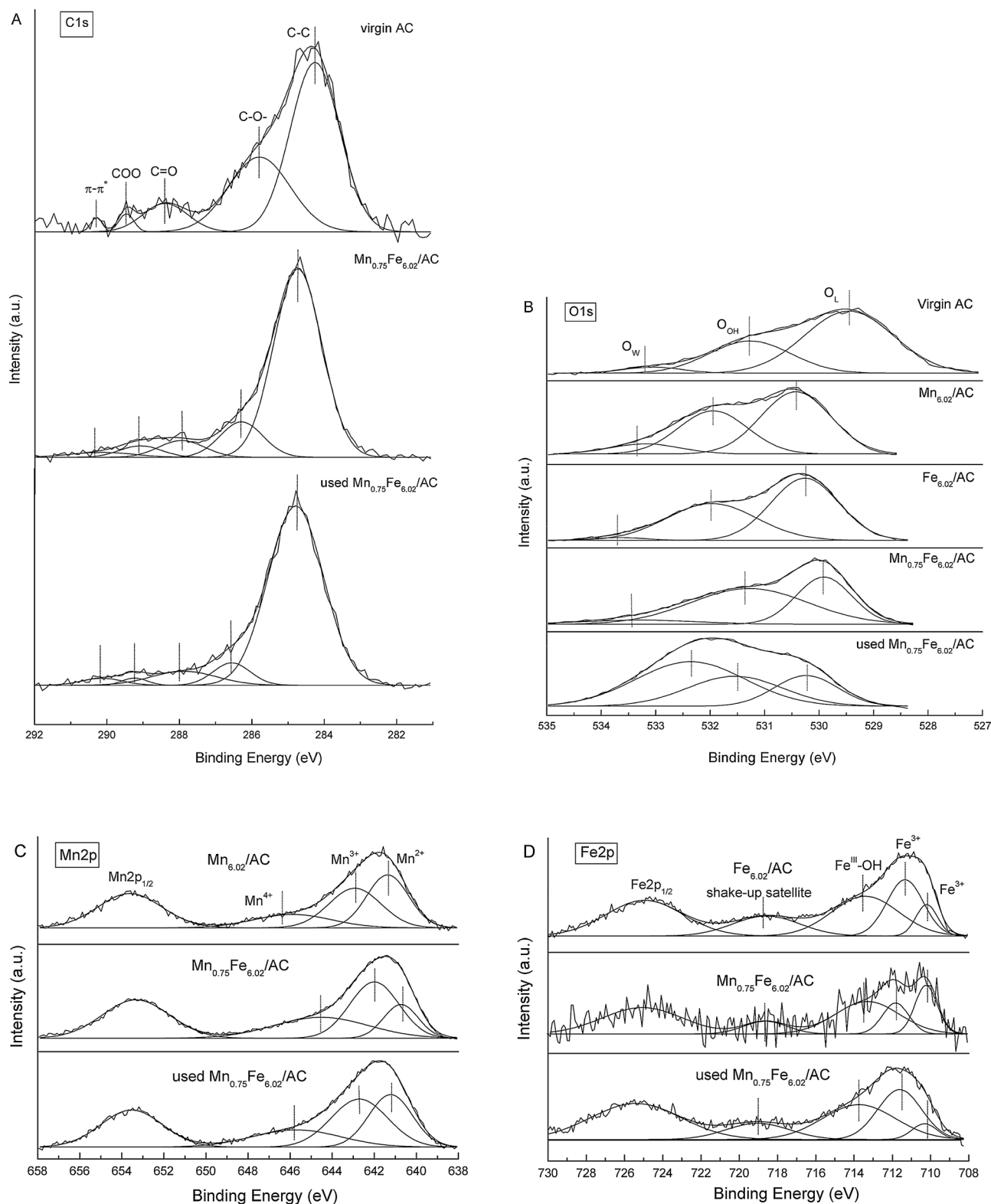
Fig. 5. XPS spectra for (A) C1s, (B) O1s, (C) Mn2p and (D) Fe2p of the samples before and after the reaction. (Reaction condition: 120 ppm HCHO, 6% O_2, total flow rate 500 mL/min, reaction temperature 300 °C).

redox property. Therefore, the effect of loading value (mass percent of metal Mn-Fe on Mn_xFe_y/AC) on E_{HCHO} was evaluated (Fig. 7). It could be seen that the loading value significantly improved the HCHO removal efficiency. In particular, E_{HCHO} initially increased remarkably, and then reached a maximum before a rapid decrease with further increase of loading value. In particular, for $Mn_{0.75}Fe_{6.02}/AC$, the catalyst,

with the best catalytic activity, exhibited the high E_{HCHO} of 98.30%, which was 8.51% higher than $Mn_{0.75}Fe_{7.42}/AC$.

Obviously, $Mn_{0.75}Fe_{6.02}/AC$ exhibited the best catalytic performance with the highest specific surface area and well-dispersed Mn-Fe oxides, which could provide more active sites for both adsorption and oxidation of HCHO. Besides, from the results of H_2-TPR, the catalytic

Table 4
The relative XPS intensity of as-prepared samples.

Relative intensity	AC	$Mn_{6.02}/AC$	$Fe_{6.02}/AC$	$Mn_{0.75}Fe_{6.02}/AC$	Used $Mn_{0.75}Fe_{6.02}/AC$
C-C(%)	57.19	–	–	74.55	81.86
C-O-(%)	31.22	–	–	12.50	6.84
C = O(%)	8.69	–	–	6.35	7.50
COO(%)	1.81	–	–	3.97	1.48
π-π^*(%)	1.09	–	–	2.32	2.32
O_L (%)	64.78	54.05	55.00	35.98	20.09
O_{OH} (%)	30.98	37.13	43.08	57.51	29.55
O_W (%)	4.24	8.83	1.92	6.51	50.36
[a] Mn^{2+}(%)	–	29.39	–	13.72	25.91
[a] Mn^{3+}(%)	–	27.47	–	32.55	30.84
[a] Mn^{4+}(%)	–	13.77	–	23.37	17.26
Mn^{4+}/Mn^{3+}	–	0.50	–	0.72	0.56
$Mn^{4+} + Mn^{3+}/Mn^{2+}$	–	1.40	–	4.08	1.86
[b]Fe^{3+}(%)	–	–	42.97	36.93	38.41
[b]Fe^{III}-OH(%)	–	–	28.07	31.39	26.93
Fe^{3+}/Fe^{III}-OH	–	–	1.53	1.17	1.43

[a] the percent of different valence of Mn in $Mn2p_{3/2}$.

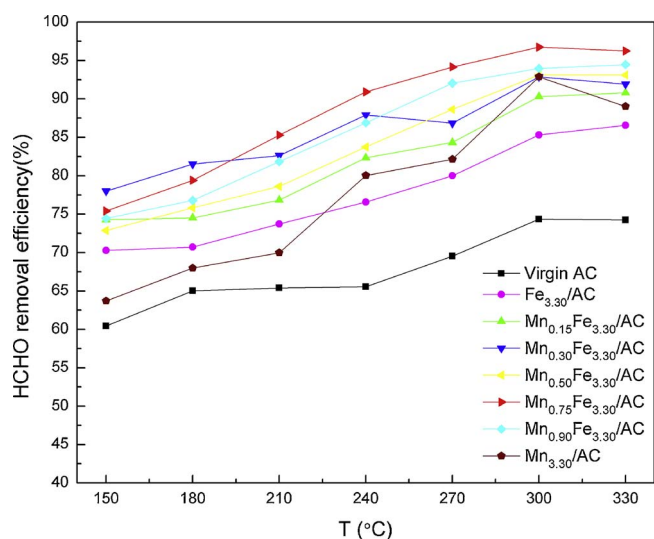[b] the percent of different state of Fe in $Fe2p_{3/2}$ and shake-up satellite.

Fig. 6. Removal of HCHO on $Mn_xFe_{3.30}/AC$ samples in simulated flue gas. (Reaction condition: 120 ppm HCHO, 6% O_2, 20 g sample, total flow rate 500 mL/min).
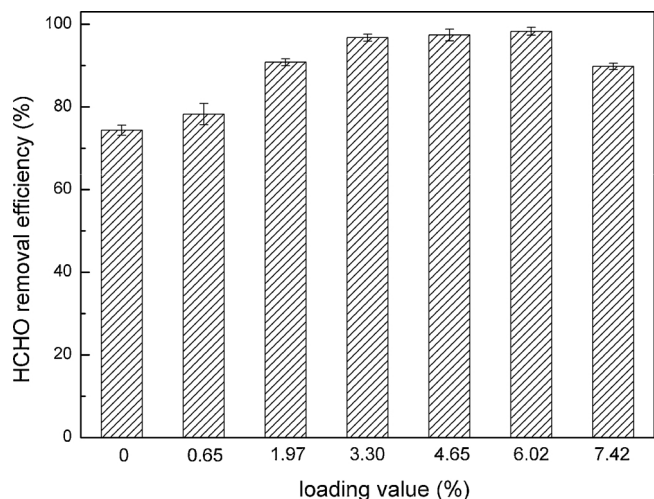

Fig. 7. Effect of loading value (y) on conversion of HCHO over $Mn_{0.75}Fe_y/AC$. (Reaction condition: 120 ppm HCHO, 6% O_2, 20 g sample, total flow rate 500 mL/min, reaction temperature 300 °C).

activity of HCHO is closely related with the reducibility and oxygen vacancies. In combination with XPS characterization, for $Mn_{0.75}Fe_{6.02}/$ AC, the high reducibility is contributed to the improvement in the mobility and amount of surface active oxygen (O_L, O_{OH}, etc.), and then facilitates a facile redox process with lower energy demand, thus leading to a promotional catalytic oxidation [62].

On the other hand, with the co-modification of Mn-Fe oxides, the increase of the amount of Mn^{4+}, Mn^{3+} and Fe^{III}-OH enhanced the adsorption and oxidation of reactants. Besides, the synergistic effect in $Mn_{0.75}Fe_{6.02}/AC$ induced the generation of surface active oxygen with high mobility and activity, thus leading to highest reducibility relative to the release of oxygen to react with HCHO and intermediates. Consequently, $Mn_{0.75}Fe_y$ exhibited excellent HCHO catalytic efficiency above 90% at 300 °C as the loading value was more than 1.97%.

3.4. Effect of gas components

3.4.1. Effect of O_2

As a crucial gas component, effect of O_2 on HCHO removal and CO_2 conversion over $Mn_{0.75}Fe_{6.02}/AC$ was investigated. As shown in Fig. 8, at the temperature window of 60–150 °C, the HCHO removal efficiency decreased in all three atmospheres, and the CO_2 conversion increased with the increasing temperature. The results above indicated that the physisorption played predominant role at low temperature and was gradually substituted by chemisorption as the temperature increased. And for higher temperature, catalytic oxidation, instead of adsorption, became the main factor influencing HCHO removal as more kinetic energy was provided by increasing temperature, which could be deduced from the higher efficiency of HCHO removal and CO_2 conversion with the presence of O_2. At the absence of O_2, $Mn_{0.75}Fe_{6.02}/AC$ still possessed relatively high activity at high temperature by the consumption of abundant surface active oxygen. This may be because that the co-modification of MnO_x and FeO_x could improve the redox properties and the mobility of the active oxygen species over the surface of catalysts. After the addition of 6% O_2, both E_{HCHO} and S_C increased sharply, while there was no evident increase of E_{HCHO} and S_C with 12% O_2/N_2. The results above indicated that gas-phase O_2 could regenerate the lattice oxygen and replenish the chemisorbed oxygen, and 6% O_2 was sufficient for the HCHO oxidation.

3.4.2. Effect of SO_2

The slight inhibitory effect of SO_2 on HCHO removal was observed (Fig. 9). E_{HCHO} were 57.35% and 52.87% with respect to 400 and 800 ppm SO_2 in the absence of O_2, respectively, which declined slightly compared with that of pure N_2. As a polar molecule, SO_2 (dipole
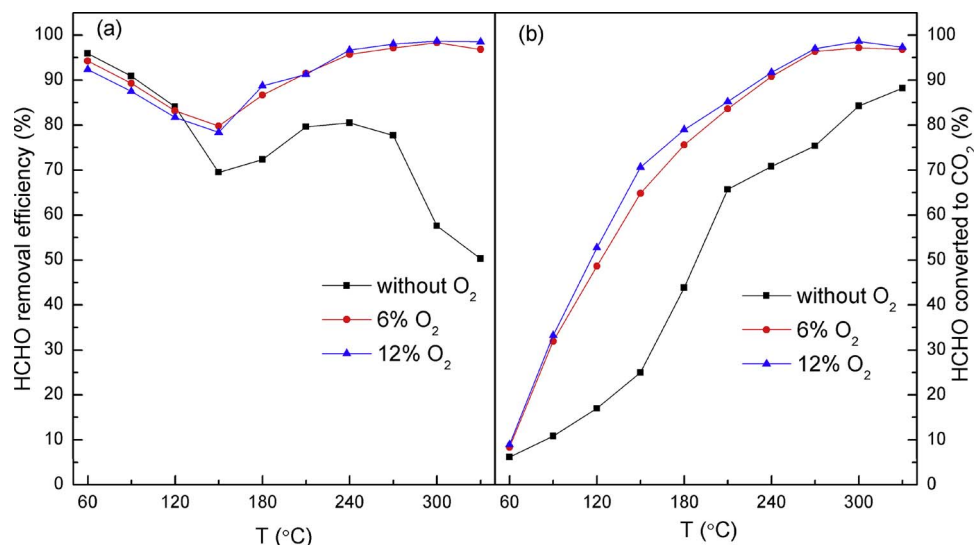
Fig. 8. HCHO removal (a) and HCHO converted to CO_2 (b) as a function of reaction temperature in simulated flue gas with different O_2 concentration for $Mn_{0.75}Fe_{6.02}/AC$. (Reaction condition: 120 ppm HCHO, 0–12% O_2, 20 g sample, total flow gas rate 500 mL/min).
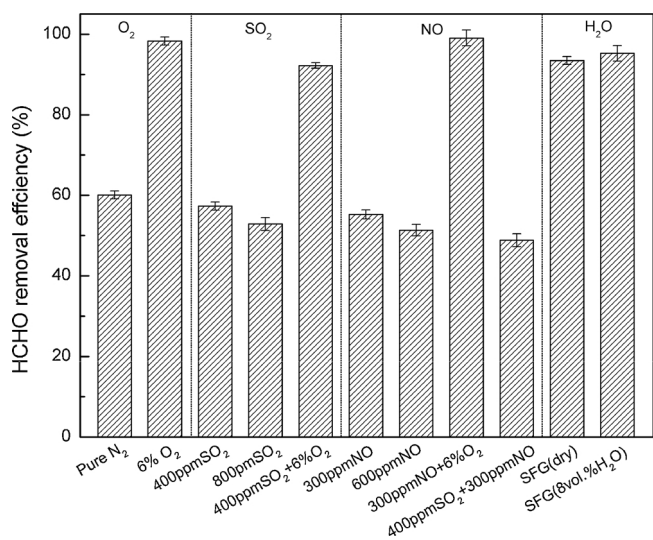

Fig. 9. Effect of flue gas components on HCHO removal over $Mn_{0.75}Fe_{6.02}/AC$. (Reaction condition: 120 ppm HCHO, 0–6% O_2, 0–800 ppm SO_2, 0–600 ppm NO, 0–8 vol.% H_2O, 20 g sample, total flow rate 500 mL/min, reaction temperature 300 °C, and SFG = 120 ppm HCHO + 300 ppm NO + 400 ppm SO_2 + 6% O_2 + N_2).

moment = 1.60D) leaned to be adsorbed by some polar or basic adsorption sites, whereas compared with the strong polarity of HCHO (dipole moment = 2.33D), there was less competition with HCHO for active sites. At the same time, SO_2 or SO_3 oxidized by surface oxygen also could react with metal oxides over AC and formed sulfite and sulfate, which not only reduced the effective active components for HCHO oxidation, but caused the blockage of micropores for the adsorption of reactant [60]. With the aid of 6% O_2, the inhibition of SO_2 was weakened as a result of the replenishment of the surface oxygen consumed by SO_2.

3.4.3. Effect of NO

As shown in Fig. 9, HCHO removal efficiencies were 55.26% and 51.35% in the presence of 300 and 600 ppm NO balanced in N_2, respectively. As we all known, with lower diameter, NO molecules could spread more quickly than HCHO to occupy active sites for the following adsorption and oxidation [64]. Moreover, NO could be oxidized by the limited surface oxygen easily to form NO_2, even NO_2^- and NO_3^- [65]. Although NO_2 possesses higher oxidizing power than O_2 for the

oxidation of VOCs, as reported in literature [65], NO still inhibited HCHO removal over $Mn_{0.75}Fe_{6.02}/AC$ with the absence of O_2 because of the overwhelming limit from NO taking up active sites and consuming active oxygen. Therefore, introducing 6% O_2 into the flue gas with 300 ppm NO balanced in N_2, E_{HCHO} was enhanced significantly to 99.05% higher than that of the absence of NO. The replenishment of active oxygen due to the presence of gas-phase O_2 produced more NO_2 as a more powerful oxidant, thus replaced or assisted O_2 for the reoxidation of the reduced metal oxides sites faster through the recycle of $NO_2 \leftrightarrow NO + O^*$ [66]. In a word, O_2 played an important role in the effect of NO on HCHO removal.

When SO_2 and NO coexisted in pure N_2, only 48.85% HCHO was removed due to the stronger competition for active sites among the reactants. With the presence of 6% O_2, a high HCHO removal efficiency of 93.45% was reached over $Mn_{0.75}Fe_9/AC$, demonstrating that $Mn_{0.75}Fe_{6.02}/AC$ has great potential in practical application. It has been reported [67] that the reaction $(NO)_{ads} + (O_2)_{ads} + (SO_2)_{ads} \rightarrow [(NO_2)(SO_3)]_{ads}$ promoted the adsorption of NO and SO_2, and then strengthened the competition for active sites between HCHO, NO and SO_2.

3.4.4. Effect of H_2O

To investigate the effect of water vapor on HCHO removal, 8 vol.% water vapor was added into the simulated flue gas (SFG) at optimal reaction temperature. As seen from Fig. 9, the addition of 8 vol.% water vapor increased the E_{HCHO} from 93.45% to 95.26%. The slight increase might be contributed to the activation of surface active oxygen (O_2^-, O^-, etc) by H_2O according to the reaction O_2^-, $O^- + H_2O \rightarrow O^* + 2-OH$, through which way the consumed hydroxyl groups could be regenerated. Chen et al. [14] also reported the positive effect of H_2O both on the formation and further oxidation of the formate intermediates, leading to an enhanced HCHO removal activity, while Raupp et al. [68] found the water vapor would block the unsaturated coordination sites via the associative and dissociative (as –OH) adsorption on reduced cations, thus leading to the dramatic loss of the catalytic activity. The results above suggest the catalyst possesses excellent H_2O durability, which is competitive in practical application on catalytic removal of HCHO, and the specific mechanism how SO_2, NO and H_2O affect the HCHO oxidation is expected to explore in our further study.

To measure the stability and selectivity of $Mn_{0.75}Fe_{6.02}/AC$ in the removal of HCHO from SFG, the oxidation of HCHO at 300 °C was conducted for 18 h, and the results are presented in Fig. 10. E_{HCHO} increased sharply from 80.35% to 95.37% in initial 8 h and then kept stable at above 95% except for a negligible fluctuation. It is worth
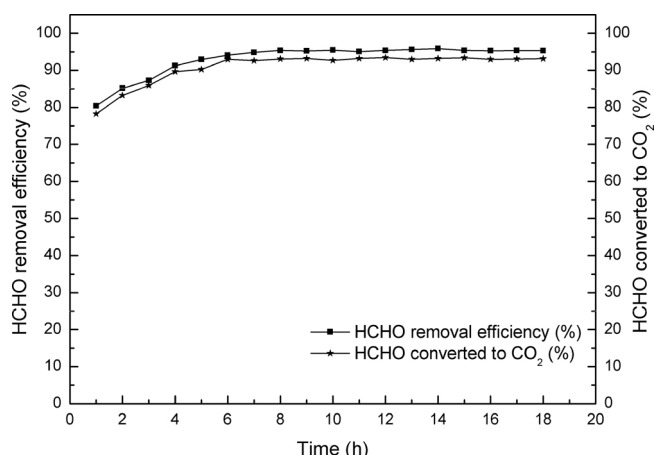
Fig. 10. Stability test of HCHO conversion over $Mn_{0.75}Fe_{6.02}/AC$. (Reaction condition: 120 ppm HCHO, 300 ppm NO, 400 ppm SO_2, 6% O_2, 8 vol.% H_2O and balance N_2, 20 g sample, total flow rate 500 mL/min, reaction temperature 300 °C).

noting that the variation of CO_2 conversion (S_C) was similar to that observed in HCHO removal, and slightly lower than HCHO removal efficiency. This suggested that a small amount of byproducts generated in HCHO oxidation, such as formate and carbonate intermediates, which agreed with the following FT-IR results and previous study [63]. It was manifested that $Mn_{0.75}Fe_{6.02}/AC$ owned an excellent stability and selectivity for the removal of HCHO from simulated flue gas, as well as good resistance to SO_2, NO and H_2O, which was significant in practical applications.

3.5. Simultaneous removal of Hg⁰ and HCHO

The simultaneous removal of Hg^0 and HCHO over $Mn_{0.75}Fe_{6.02}/AC$ were investigated at the temperature of 150–330 °C, and the results were shown in Fig. 11. It is obvious that Hg^0 removal efficiency decreased with the increasing temperature from 150 to 210 °C and then increased sharply to reach the highest removal efficiency of 77.51% at 270 °C in the presence of HCHO. As shown in Fig. 11B, the removal of mercury over samples occurred as the synergy of adsorption and oxidation, where adsorption acted as the removal mechanism at lower temperature, and then was substituted by the oxidation with the increasing reaction temperature, which was in accordance with Zhao et. al [69]. Besides, oxidation was in the lead of HCHO removal, and increased as the temperature increased. Therefore, 270 °C was chosen as the optimal temperature for the simultaneous removal of Hg^0 and HCHO. Furthermore, a connection between Hg^0 and HCHO removal was also studied. It was obvious that the addition of HCHO significantly inhibited the removal of mercury due to the competition of active sites. However, after introducing Hg^0, a slight decrease lower than 6% for E_{HCHO} was observed, which might be the mercury concentration (90 μg/m³) was extremely too small compared with HCHO concentration (120 ppm).

3.6. Mechanism discussion

The surface of $Mn_{0.75}Fe_{6.02}/AC$ before and after exposure to HCHO was investigated by XPS. As shown in Fig. 5A, after treated with HCHO, C=O showed a slight increase compared with the fresh sample, which might be ascribe to the adsorption of HCHO on samples and/or the oxidation of HCHO to formate species. And the decrease of C-O- and COO, as well as the increase of C—C, indicated the participation of surface adsorbed oxygen during the oxidation of HCHO. The results above elucidated the oxygen-containing functional groups and π-π* interactions not only played an important role in the coating of active components on the surface of AC, but also participated in the oxidation
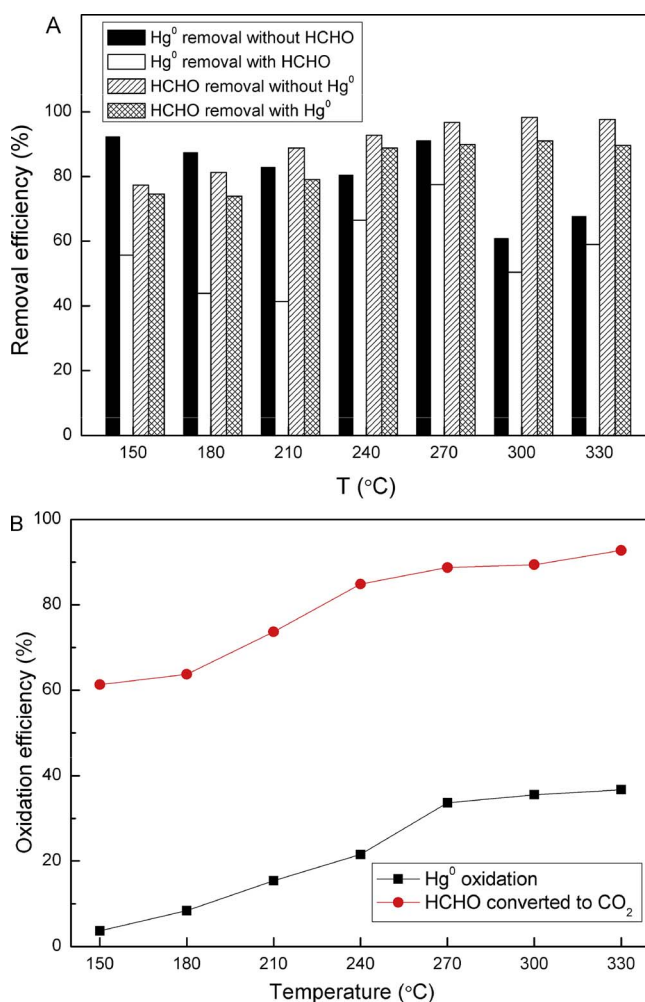

Fig. 11. Simultaneous (A) removal and (B) oxidation of Hg^0 and HCHO over $Mn_{0.75}Fe_{6.02}/AC$. (Reaction condition: 120 ppm HCHO, 90 μg/m³ Hg^0, 6% O_2, 20 g sample, total flow rate 500 mL/min).

of HCHO. For O1s, the ratio of O_L and O_{OH} over used $Mn_{0.75}Fe_{6.02}/AC$ exhibited a sharp decrease, especially for O_{OH}, indicating that both O_L and O_{OH} participated in HCHO removal. Xu et al. [70] also reported that abundant hydroxyls could offer more adsorption sites for HCHO, and facilitate the oxidation of formate species into CO_2 and H_2O. Besides, an increase of 43.85% for the ratio of O_W revealed that an amount of H_2O was generated during HCHO decomposition and oxidation.

The oxidation states of the metal elements over fresh and used $Mn_{0.75}Fe_{6.02}/AC$ were also studied. Comparing with fresh $Mn_{0.75}Fe_{6.02}/AC$, Mn^{4+} and Mn^{3+} decreased sharply, especially for Mn^{4+}, while more Mn^{2+} was generated after treated with the reaction (Table 4), demonstrating that the reaction of $Mn^{4+} \rightarrow Mn^{3+} \rightarrow Mn^{2+}$ occurred, and then facilitated the oxidation of HCHO. Besides, the ratio of Fe^{3+}/Fe^{III}-OH for $Mn_{0.75}Fe_{6.02}/AC$ increased from 1.17 to 1.43 (Table 4), indicating that the −OH bonded with Fe^{3+} participated in the oxidation of HCHO, further confirming the promotion of −OH in the process of HCHO removal. It has also been reported that the promotion of Fe^{III}-OH was attributed to the hydrogen-bonding interaction between the H atoms of Fe^{III}-OH and the O atoms of HCHO molecules [71].

To illustrate the oxidation mechanism of HCHO over $Mn_{0.75}Fe_{6.02}/AC$, the FT-IR spectra of $Mn_{0.75}Fe_{6.02}/AC$ with exposure to HCHO with different atmosphere and different temperatures were investigated (Fig.12). Upon exposure to 120 ppm $HCHO/N_2$ at room temperature for 2 h (curve b), bands at 3747, 2300–2400, 1575, 1134, 600–700 cm⁻¹ were observed. According to literatures, the band at 1134 cm⁻¹ was corresponded to molecularly adsorbed formaldehyde [72,73], which

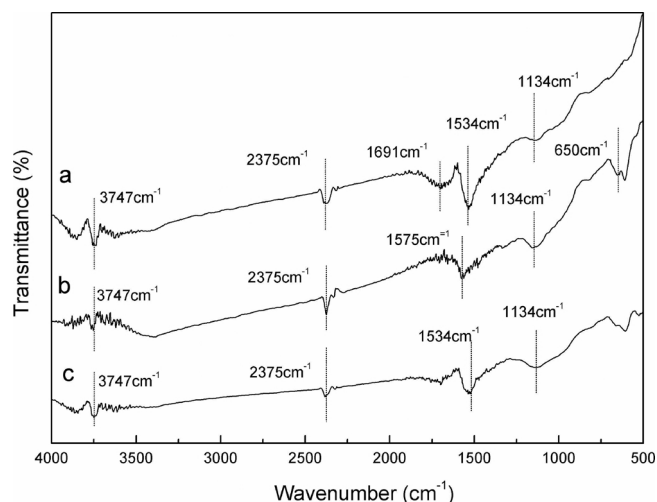**Fig. 12.** FT-IR spectra of $Mn_{0.75}Fe_{6.02}/AC$ under different conditions: a. 120 ppm HCHO + 6% O_2 + N_2 at 300 °C; b. 120 ppm HCHO + N_2 at room temperature; c. 120 ppm HCHO + 6% O_2 + N_2 at room temperature.

suggested that HCHO adsorbed on $Mn_{0.75}Fe_{6.02}/AC$ catalyst surface firstly. The bands related to the formation of formate species adsorbed on the catalyst surface at 3747, 1575 and 600–700 cm^{-1} were assigned to the isolated −OH of formic acid, the asymmetric stretching vibration of COO (ν_{as}(COO-)) of formate and strong C-H deformation, respectively [14,74]. Moreover, the peak of adsorbed CO_2 (bands at 2300–2400 cm^{-1}) might be partly generated during HCHO oxidation process, which was further proved by CO_2 detected in outlet flue gas. It indicated that the $Mn_{0.75}Fe_{6.02}/AC$ could act as an efficient catalyst with sufficient oxygen functional groups for the oxidation of HCHO even in the absence of O_2 [14]. Upon introducing O_2 into the feed stream (curve c), similar bands were observed. However, the band at 1575 cm^{-1} (ν_{as}(COO-)) disappeared and the relative intensity of bands at 600–700 cm^{-1} was weakened. And the band at 1534 cm^{-1} was assigned to the asymmetric virbration of carbonate species [74], indicative of that the gas-phase O_2 facilitated the further oxidation of formate species through the supplement of surface active oxygen. For curve a, the intensity of band at 1134 cm^{-1} weakened and band at

1534 cm^{-1} strengthened. Besides, the band at 1691 cm^{-1} was also ascribed to carbonate species. With the increase of temperature, part of adsorbed HCHO could be oxidized to carbonate species rapidly, and then facilitated the oxidation of HCHO into CO_2, which was consistent with the experiment results.

A possible mechanism of HCHO removal on the Mn_xFe_y/AC is proposed based on the obtained results and previous studies, as shown in Fig.13. With the co-modification of Mn-Fe oxides, Mn_xFe_y/AC owned more active surface oxygen, more Mn atoms with high valence and Fe^{3+} bonded with −OH, and the good reducibility due to the synergy of MnO_x and FeO_x. Firstly, HCHO molecule was adsorbed on the surface of catalyst via the hydroxyl groups and some other active sites, and abundant active surface oxygen (O^*) released via the redox cycles of Fe^{3+}/Fe^{2+} and $Mn^{4+}/Mn^{3+}/Mn^{2+}$, as well as chemisorbed oxygen of surface functional groups over activated coke. Secondly, the nucleophilic O^* attracted C-H of adsorbed formaldehyde molecule to produce the formate species, which was proved by the peaks ascribed to C-H deformation and formate species in FT-IR, as well as the C1s XPS spectra. Meanwhile, the oxygen vacancy was formed and then filled via the decomposition of gas phase O_2 molecule rapidly. Subsequently, the active hydroxyl radicals further oxidized formate intermediate into adsorbed CO_2 and H_2O. During the process, part of formate species were converted into carbonate species after losing another −H and then were further oxidized into CO_2 and H_2O, which was also detected in FT-IR characterization. Moreover, the lost −H could react with the unbonded −OH adsorbed on the sample surface to generate H_2O. Finally, the generated $(CO_2)_{ads}$ and $(H_2O)_{ads}$ desorbed from the sample surface.

4. Conclusion

The Mn_xFe_y/AC samples were prepared by impregnation method for the HCHO removal. The superior HCHO removal efficiency above 90% was obtained over $Mn_{0.75}Fe_{3.30}/AC$ at the temperature window of 240–330 °C, and the maximum of that reached 98.30% over $Mn_{0.75}Fe_{6.02}/AC$ at 300 °C. Besides, $Mn_{0.75}Fe_{6.02}/AC$ also exhibited excellent stability and selectivity during 18 h test, and had potential in the simultaneous removal of HCHO and Hg^0. SO_2 and NO showed an inhibitory effect on HCHO removal without O_2 due to the competitive adsorption. However, gas-phase O_2 regenerated the lattice oxygen and
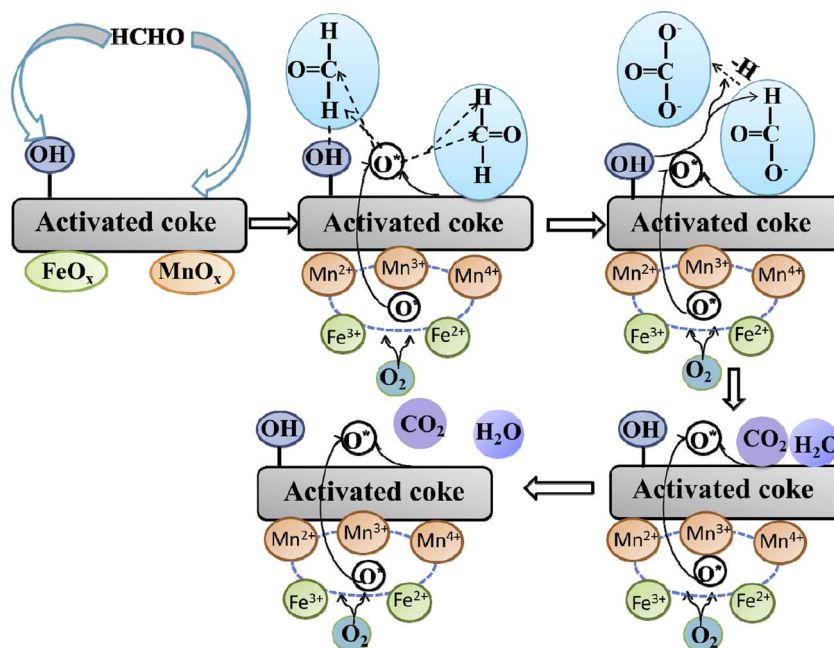

Fig. 13. The proposed mechanism of HCHO removal process over Mn_xFe_y/AC.

supplemented the chemisorbed oxygen, facilitating the removal of HCHO. Therefore, with the addition of O_2, the negative effect of SO_2 was weakened, and NO promoted HCHO removal due to the generation of abundant NO_2, which possessed higher oxidizing power than O_2. H_2O further enhanced the HCHO oxidation via the supplement of the consumed $-OH$. In addition, characterization results demonstrated that $Mn_{0.75}Fe_{6.02}/AC$ possessed large surface area, high dispersion of active components and higher reducibility, which facilitated the removal of HCHO. XPS results indicated that oxygen-containing groups, such as C-O- and COO-, abundant active surface oxygen and $-OH$, played an important role in both adsorption and oxidation of HCHO, as well as the redox cycle of Fe^{3+}/Fe^{2+} and $Mn^{4+}/Mn^{3+}/Mn^{2+}$. Moreover, based on FT-IR results, HCHO was adsorbed on the samples via $-OH$ and other active sites, and then oxidized into formate and carbonate intermediates, finally further oxidized into CO_2 and H_2O. Further studies to investigate the mechanism how NO, SO_2 and H_2O affect HCHO removal and the simultaneous removal of HCHO and Hg^0 are warranted.

Acknowledgements

References

[1] C. Deng, Q. Huang, X. Zhu, Q. Hu, W. Su, J. Qian, L. Dong, B. Li, M. Fan, C. Liang, Appl. Surf. Sci. 389 (2016) 1033–1049.
[2] S. Lu, K. Li, F. Huang, C. Chen, B. Sun, Appl. Surf. Sci. 400 (2017) 277–282.
[3] B.B. Chen, X.B. Zhu, M. Crocker, Y. Wang, C. Shi, Appl. Catal. B: Environ. 154–155 (2014) 73–81.
[4] L. Ma, D. Wang, J. Li, B. Bai, L. Fu, Y. Li, Appl. Catal. B: Environ. 148–149 (2014) 36–43.
[5] J. Yu, X. Li, Z. Xu, W. Xiao, Environ. Sci. Technol. 47 (2013) 9928–9933.
[6] M. Chidambaram, S. Selvakumar, T. Tamil Selvi, A.P. Singh, J. Mol. Catal. A 245 (2006) 69–77.
[7] G.K. Zhang, X. Qin, Mater. Res. Bull. 48 (2013) 3743–3749.
[8] P. Liu, H. He, G. Wei, X. Liang, F. Qi, F. Tan, W. Tan, J. Zhu, R. Zhu, Appl. Catal. B: Environ. 182 (2016) 476–484.
[9] W.J. Liang, J. Li, J.X. Li, T. Zhu, Y.Q. Jin, J. Hazard. Mater. 175 (2010) 1090–1095.
[10] Z. Xu, N. Qin, J. Wang, H. Tong, Bioresour. Technol. 101 (2010) 6930–6934.
[11] J.I. Gutierrez-Ortiz, B. de Rivas, R. Lopez-Fonseca, S. Martin, J.R. Gonzalez-Velasco, Chemosphere 68 (2007) 1004–1012.
[12] L. Qi, B. Cheng, J. Yu, W. Ho, J. Hazard. Mater. 301 (2016) 522–530.
[13] D. Li, G. Yang, P. Li, J. Wang, P. Zhang, Catal. Today (2016).
[14] B.B. Chen, C. Shi, M. Crocker, Y. Wang, A.M. Zhu, Appl. Catal. B: Environ. 132–133 (2013) 245–255.
[15] Z. Tang, W. Zhang, Y. Li, Z. Huang, H. Guo, F. Wu, J. Li, Appl. Surf. Sci. 364 (2016) 75–80.
[16] S. Colussi, M. Boaro, L. de Rogatis, A. Pappacena, C. de Leitenburg, J. Llorca, A. Trovarelli, Catal. Today 253 (2015) 163–171.
[17] B.B. Chen, X.B. Zhu, M. Crocker, Y. Wang, C. Shi, Catal. Commun. 42 (2013) 93–97.
[18] B. Liu, Y. Liu, C. Li, W. Hu, P. Jing, Q. Wang, J. Zhang, Appl. Catal. B: Environ. 127 (2012) 47–58.
[19] X. Tang, J. Chen, X. Huang, Y. Xu, W. Shen, Appl. Catal. B: Environ. 81 (2008) 115–121.
[20] Y. Yu, T. Wang, Y. Fu, W. Su, J. Hu, Int. J. Hydrogen Energy 39 (2014) 17617–17621.
[21] Y. Ma, G. Zhang, Chem. Eng. J. 288 (2016) 70–78.
[22] H. Chen, Z. Rui, X. Wang, H. Ji, Catal. Today 258 (2015) 56–63.
[23] G.K. Zhang, Q. Xiong, W. Xu, S. Guo, Appl. Clay. Sci. 102 (2014) 231–237.
[24] S. Shin, J. Song, J. Hazard. Mater. 194 (2011) 385–392.
[25] Q. Wen, C. Li, Z. Cai, W. Zhang, H. Gao, L. Chen, G. Zeng, X. Shu, Y. Zhao, Bioresour. Technol. 102 (2011) 942–947.
[26] W.D.P. Rengga, A. Chafidz, M. Sudibandriyo, M. Nasikin, A.E. Abasaeed, J. Environ. Chem. Eng. 5 (2017) 1657–1665.
[27] J. Li, N. Kobayashi, Y. Hu, Chem. Eng. Process. 47 (2008) 118–127.
[28] K. Jastrząb, Fuel Process. Technol. 101 (2012) 16–22.
[29] F. Sun, J. Gao, X. Liu, X. Tang, S. Wu, Appl. Surf. Sci. 357 (2015) 1895–1901.
[30] Y. Itaya, K. Kawahara, C.W. Lee, J. Kobayashi, N. Kobayashi, S. Hatano, S. Mori, Fuel 88 (2009) 1665–1672.
[31] S. Ogriseck, G.P.G. Vanegas, Chem. Eng. J. 160 (2010) 641–650.
[32] S.S. Tao, C.T. Li, X.P. Fan, G.M. Zeng, P. Lu, X. Zhang, Q.B. Wen, W.W. Zhao, D.Q. Luo, C.Z. Fan, Chem. Eng. J. 210 (2012) 547–556.
[33] H. Wu, C.T. Li, L.K. Zhao, J. Zhang, G. Zeng, Y. Xie, X. Zhang, Y. Wang, Energy Fuel 29 (2015) 6747–6757.
[34] Y. Wang, C.T. Li, L.K. Zhao, Y. Xie, X. Zhang, G. Zeng, H. Wu, J. Zhang, Environ. Sci. Pollut. R. 23 (2016) 5099–5110.
[35] K. Tong, A. Lin, G. Ji, D. Wang, X. Wang, J. Hazard. Mater. 308 (2016) 113–119.
[36] M.H. Zhang, Q.L. Zhao, Z.F. Ye, J. Environ. Sci. 23 (2011) 1962–1969.
[37] B. Zhao, X. Liu, Z. Zhou, H. Shao, M. Xu, Chem. Eng. J. 284 (2016) 1233–1241.
[38] Y. Xie, C. Li, L. Zhao, J. Zhang, G. Zeng, X. Zhang, W. Zhang, S. Tao, Appl. Surf. Sci. 333 (2015) 59–67.
[39] X. Peng, H. Yi, X. Tang, K. Li, Res. Chem. Intermed. 41 (2013) 213–222.
[40] S.A.C. Carabineiro, N. Bogdanchikova, P.B. Tavares, J.L. Figueiredo, RSC Adv. 2 (2012) 2957.
[41] X. Liang, P. Liu, H. He, G. Wei, T. Chen, W. Tan, F. Tan, J. Zhu, R. Zhu, J. Hazard. Mater. 306 (2016) 305–312.
[42] S.C. Kim, W.G. Shim, Appl. Catal. B: Environ. 98 (2010) 180–185.
[43] H. Tian, J. He, X. Zhang, L. Zhou, D. Wang, Microporous Mesoporous Mater. 138 (2011) 118–122.
[44] R. Lin, W.-P. Liu, Y.-J. Zhong, M.-F. Luo, Appl. Catal. A: Gen. 220 (2001) 165–171.
[45] F.F.A. Parmaliana, Appl. Catal. A: Gen. 226 (2002).
[46] J. He, Y. Li, D. An, Q. Zhang, Y. Wang, J. Nat. Gas Chem. 18 (2009) 288–294.
[47] L.K. Zhao, C.T. Li, S.H. Li, Y. Wang, J. Zhang, T. Wang, G. Zeng, Appl. Catal. B: Environ. 198 (2016) 420–430.
[48] C. He, B. Shen, B. Chi, F. Li, Chem. Eng. J. 300 (2016) 1–8.
[49] Y.C. Xie, Y.Q. Tang, Adv. Catal. 37 (1990) 1–43.
[50] M.H. Castaño, R. Molina, S. Moreno, Appl. Catal. A: Gen. 492 (2015) 48–59.
[51] J. Zhou, L. Zhao, Q. Huang, R. Zhou, X. Li, Catal. Lett. 127 (2008) 277–284.
[52] G. Zhang, Z. Li, H. Zheng, T. Fu, Y. Ju, Y. Wang, Appl. Catal. B: Environ. 179 (2015) 95–105.
[53] D. Li, G. Yang, P. Li, J. Wang, P. Zhang, Cataly. Today 277 (2016) 257–265.
[54] C. Ma, D. Wang, W. Xue, B. Dou, H. Wang, Z. Hao, Environ. Sci. Technol. 45 (2011) 3628–3634.
[55] S. Biniak, G. Szymański, J. Siedlewski, A. Świtkowski, Carbon 35 (1997) 1799–1810.
[56] Y. Huang, J. Tang, L. Gai, Y. Gong, H. Guan, R. He, H. Lyu, Chem. Eng. J. 319 (2017) 229–239.
[57] J. Deng, S. He, S. Xie, H. Yang, Y. Liu, G. Guo, H. Dai, Environ. Sci. Technol. 49 (2015) 11089–11095.
[58] M.V. Gallegos, M.A. Peluso, E. Finocchio, H.J. Thomas, G. Busca, J.E. Sambeth, Chem. Eng. J. 313 (2017) 1099–1111.
[59] D. Jampaiah, S.J. Ippolito, Y.M. Sabri, B.M. Reddy, S.K. Bhargava, Catal. Sci. Technol. 5 (2015) 2913–2924.
[60] J.J. Sheng, C.T. Li, L.K. Zhao, X.Y. Du, L. Gao, G. Zeng, Fuel 197 (2017) 397–406.
[61] J.R. Li, J.S. Chen, Y.K. Yu, C. He, J. Ind. Eng. Chem 25 (2015) 352–358.
[62] S.M. Li, Q.L. Hao, R.Z. Zhao, D.L. Liu, H.Z. Duan, B. J. Dou. Chem. Eng. J. 285 (2016) 536–543.
[63] G.Y. Popova, T.V. Andrushkevich, E.V. Semionova, Y.A. Chesalov, L.S. Dovlitova, V.A. Rogov, V.N. Parmon, J. Mol. Catal. A 283 (2008) 146–152.
[64] H. Li, C.Y. Wu, Y. Li, L. Li, Y. Zhao, J. Zhang, J. Hazard. Mater. 243 (2012) 117–123.
[65] A. Aissat, D. Courcot, R. Cousin, S. Siffert, Catal. Today 176 (2011) 120–125.
[66] F. Bertinchamps, M. Treinen, N. Blangenois, E. Mariage, E. Gaigneaux, J. Catal. 230 (2005) 493–498.
[67] G.B. Raupp, J.A. Dumisec, J. Phys. Chem. 89 (1985) 5240–5246.
[68] Y. Guo, Y. Li, T. Zhu, M. Ye, Energy Fuel 27 (2013) 360–366.
[69] B. Zhao, H.H. Yi, X.L. Tang, Q. Li, D.D. Liu, F.Y. Gao, Chem. Eng. J. 286 (2016) 585–593.
[70] Z. Xu, J. Yu, M. Jaroniec, Appl. Catal. B: Environ. 163 (2015) 306–312.
[71] Z. Xu, J. Yu, W. Xiao, Chem-Eur. J. 19 (2013) 9592–9598.
[72] T. Kecskés, J. Raskó, J. Kiss, Appl. Catal. A: Gen. 273 (2004) 55–62.
[73] H. Li, G. Qi, X. Tana, X. Zhang, W. Huang, W. Li, Shen, Appl. Catal. B: Environ. 103 (2011) 54–61.
[74] G.B. Elisabetta Finocchio, Catal. Today 70 (2001) 213–225.